

Dual-Wideband Low-Profile Three-Notch Patch Antenna With Indirect Differential Feeding for 5G Millimeter-Wave Applications

Byeongjin Kim, *Graduate Student Member, IEEE*, and Jungsuek Oh, *Senior Member, IEEE*

Abstract—This study presents a dual-wideband, low-profile antenna designed using novel design approaches, operating across the full 5G millimeter-wave bands around 28 GHz and 38.5 GHz. It covers n257, n258, n259, n260, and n261, spanning a total range of 24.25–29.5 GHz and 37–43.5 GHz. The proposed design incorporates a novel three-notch patch (TNP) antenna and an indirect differential feeding (IDF) configuration. The center-located hyperbolic notch and IDF, with the aid of two side-located rectangular notches for higher-band impedance matching, enable dual-wideband operation while also providing high cross-polarization discrimination. The simulated 2:1 VSWR bandwidth of the proposed TNP antenna is 24.2–29.6 GHz (20.1%) and 37.0–44.0 GHz (17.3%). During the fabrication of the array, a compact balun was designed and integrated into the proposed TNP antenna because no commercial RFIC fully covering the n257–n261 bands was available at the lab stage. The measured bandwidth of 20.5% in the lower band and 15.7% in the higher band confirmed its dual-wide bandwidth characteristic.

Index Terms—Dual-Wideband, Three-notch Patch (TNP) Antenna, Indirect Differential Feeding (IDF), 5G, Millimeter-wave (mmWave).

I. INTRODUCTION

SINCE the first commercialization of 5G millimeter-wave (mmWave) communication, design technologies for 5G mmWave antennas and metasurfaces have matured, targeting various frequency bands around 28 GHz and 38.5 GHz [1]–[19]. Over time, the operating frequencies of 5G RFICs from leading global companies have expanded beyond the commonly used bands of 26.5–29.5 GHz (n257, n261) and 37–40 GHz (n260) to also include 24.25–27.5 GHz (n258) and 39.5–43.5 GHz (n259), in order to meet the diverse requirements of different countries [1]. However, with a few exceptions [11], [12], most existing 5G mmWave dual-band or wideband antennas do not cover the n258 or n259 bands [13]–[19], leading to a critical issue where the antenna performance fails to keep up with the capabilities of RFICs.

Manuscript received O OO 2025; revised O OO 2025; accepted O OO 2025. Date of publication O OO 2025; date of current version O OO 2025. This work was supported by an Institute of Information and Communications Technology Planning and Evaluation (IITP) through the Korean Government [Ministry of Science and ICT (MSIT)], “Innovative Fusion Technologies of Intelligent Antenna Material/Structure/Network for THz 6G,” under Grant 2021-0-00763. (Corresponding author: Jungsuek Oh.).

Byeongjin Kim and Jungsuek Oh are affiliated with the Institute of New Media and Communications (INMC), Department of Electrical and Computer Engineering, Seoul National University, Seoul 08826, South Korea (e-mail: jungsuek@snu.ac.kr).

Color versions of one or more figures in this article are available at OOO Digital Object Identifier OOO.

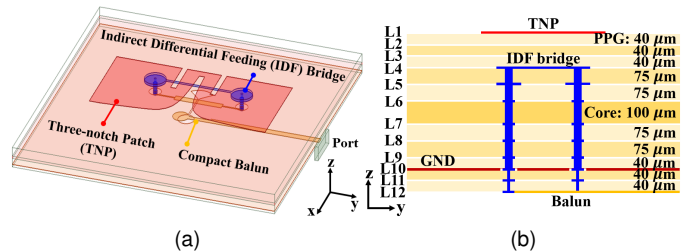


Fig. 1. Illustration of (a) the three-notch patch (TNP) antenna with an indirect differential feeding (IDF) bridge, and (b) the PCB stackup.

Present antennas that fully [11], [12] or nearly [13] cover the n257–n261 bands have been designed using different approaches. In [11], the bandwidth of dipole and shorted patch antennas was widened by placing parasitic elements around the elements. In [12], grounded dipole antennas with baluns and parasitic patches were designed. In [13], various characteristic modes were induced by a slotted patch antenna and utilized.

Meanwhile, the use of differential feeding for antennas enables wideband operation in 5G millimeter-wave bands [20]–[24], helps achieve a symmetric radiation pattern in the E-plane, and is preferred when integrated with differential circuit components. Indirect feeding, such as proximity coupling or L-probe, is also commonly used for multi-band or wideband operation [14], [25], [26].

We present a dual-wideband, low-profile antenna with novel design approaches that fully covers the 5G mmWave n257–n261 bands. The configuration of a three-notch patch (TNP) antenna and an indirect differential feeding (IDF) mechanism is demonstrated. The center-located hyperbolic notch and IDF enable wide-band operation while also providing high cross-polarization discrimination (XPD). Meanwhile, the two side-located rectangular notches enhance the impedance matching of the IDF in the higher band, ensuring dual-wideband performance. During the fabrication of the array, the TNP antenna was integrated with a compact balun because no RFIC fully covering n257–n261 was available at the lab stage.

II. ANTENNA CONFIGURATION AND MECHANISM

A. Three-notch Patch (TNP) Antenna

Fig. 1 shows the proposed TNP antenna, its main components (the TNP, an IDF bridge, and a compact balun), and the PCB stackup information. The simulation results shown in Fig. 4, 5, and 6 are based on the original TNP antenna (without the

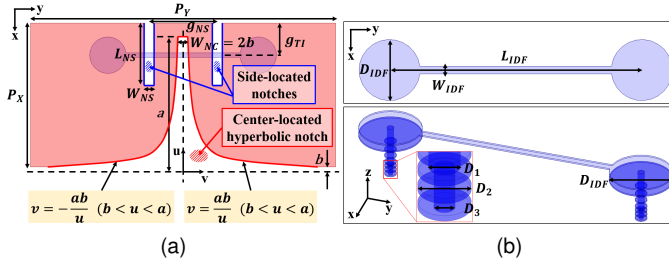


Fig. 2. Design parameters of the proposed antenna components: (a) The TNP in L1 with the IDF bridge in L4-L9. The assigned design parameter values (in mm) are $P_X=3.15$, $P_Y=6.7$, $L_{NS}=1.35$, $g_{NS}=1.7$, $W_{NS}=0.2$, $W_{NC}=2b=0.2$, $a=3$, $b=0.1$, $g_{TI}=0.7$, $D_{IDF}=1$, $L_{IDF}=3.3$, $W_{IDF}=0.1$, $D_1=0.09$, $D_2=0.15$, and $D_3=0.06$.

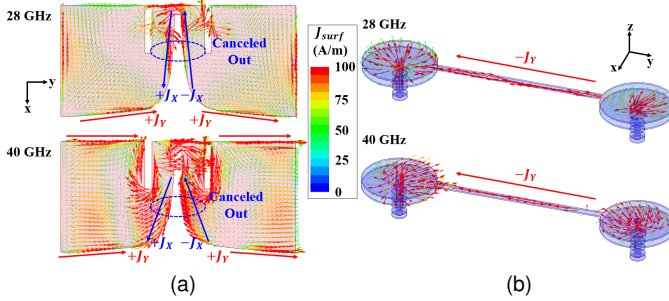


Fig. 3. Surface current distribution on (a) the TNP in L1 and (b) the IDF bridge in L4.

balun), which in simulation is excited by two ports at a 180-degree phase difference. Fig. 1(b) illustrates that the proposed antenna was fabricated using a stackup-PCB process featuring fine metal patterning and utilizing a total of 12 metal layers (L1 to L12), each copper layer being $18 \mu\text{m}$ thick. The thicknesses of the prepreg and core layers are indicated in the figure. The relative permittivity and loss tangent for the prepreg layers are 3.2 and 0.004, respectively, while those for the core layer are 3.4 and 0.004. The total thickness of the proposed antenna is $856 \mu\text{m}$. Fig. 2 shows the configuration of the TNP and IDF bridge, along with their design parameters.

B. Mechanism of Dual-Wideband and High XPD

Fig. 3(a) shows the surface current distribution on the TNP antenna at 28 GHz and 40 GHz. It can be observed that the varying length of the surface current path, formed along the contour of the center-located hyperbolic notch, enables dual-wideband operation. Notably, the two side-located rectangular notches are strongly coupled with the surface currents at 40 GHz, indicating the importance of these side notches for impedance matching in the higher band. The proposed TNP antenna also achieves high XPD by canceling out radiation from cross-polarized surface currents, as shown in Fig. 3(a). The long surface current path formed on the IDF bridge, shown in Fig. 3(b), also contributes to high XPD by constraining the orientation of most surface currents on the TNP.

Fig. 4 illustrates the influence of the two side-located notches. While the center notch enables wideband operation, the side notches facilitate dual-band operation by dramatically improving impedance matching at the higher band.

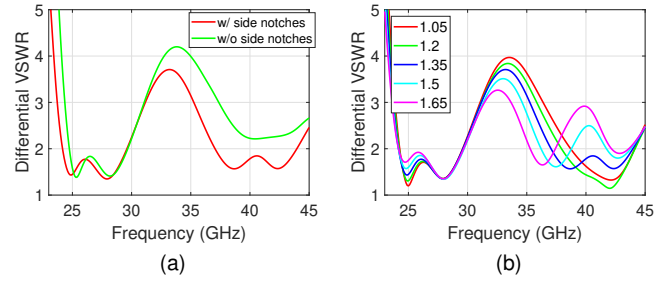


Fig. 4. Simulated differential VSWR: (a) with and without the two side notches, and for a variation in (b) L_{NS} (units: mm).

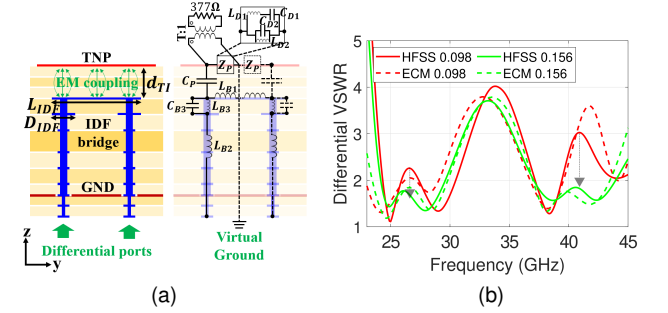


Fig. 5. (a) Illustration of the electromagnetic (EM) coupling between the TNP antenna and the IDF bridge, along with the corresponding equivalent circuit model. The optimized circuit parameter values are as follows: $(L_{B1}, L_{B2}, L_{B3}, R_{LB2}, R_{LB3}, L_{D1}, L_{D2}, C_P, C_{B3}, C_{D1}, C_{D2}, T)=(14, 0.6, 0.12, 9.3, 3.56, 9.3, 0.30, 0.052, 41.9, 190.4, 72.9, 518.9, 0.364)$ where the units are nH, Ω , and fF, respectively. (b) Differential VSWR results obtained from HFSS and equivalent circuit simulations for varying d_{TI} (in mm). The case with $d_{TI} = 0.156$ corresponds to the optimized configuration, whereas $d_{TI} = 0.098$ represents a comparative case with updated circuit parameters: $(L_{B2}, L_{D1}, L_{D2}, C_P, C_{D1})=(0.65, 0.196, 0.048, 46.1, 72.9)$.

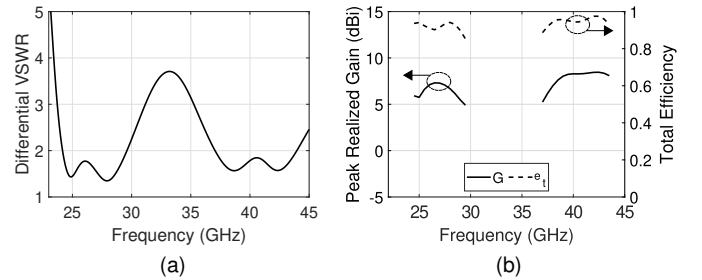


Fig. 6. Simulated (a) differential VSWR, and (b) peak gain and total efficiency versus frequency for the TNP antenna element.

Fig. 5(a) demonstrates the electromagnetic (EM) coupling between the TNP antenna and the IDF bridge, which is significantly influenced by three design parameters: D_{IDF} , d_{TI} , and L_{IDF} . The equivalent circuit of the TNP antenna is also shown in the figure. The circuit parameters exhibit complex variations in response to changes in the actual design parameters of the TNP antenna. For example, Fig. 5(b) shows the effect of d_{TI} on the differential VSWR by comparing both HFSS and circuit simulations.

Based on these findings, the final design parameter values have been determined and are shown in Fig. 2. Fig. 6(a) shows that the proposed TNP antenna achieves a wide dual-band 2:1

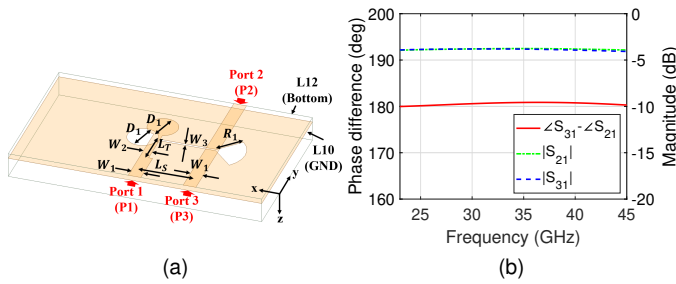


Fig. 7. (a) Illustration of the compact balun, and (b) simulated phase difference ($\angle S_{21} - \angle S_{31}$) and magnitudes $|S_{21}|$ and $|S_{31}|$. The assigned design parameter values (in mm) are $D_1=0.3$, $R_1=0.6$, $L_T=0.8$, $L_S=1.085$, $W_1=0.25$, $W_2=0.17$, and $W_3=0.05$.

VSWR bandwidth of 24.2–29.6 GHz (20.1%) and 37.0–44.0 GHz (17.3%), fully covering the target 5G mmWave bands around 28 GHz and 38.5 GHz (n257–n261), as intended. Fig. 6(b) shows that the TNP antenna provides peak gains of 7.76 dBi at 26.5 GHz and 8.53 dBi at 40.0 GHz in the lower and higher bands, respectively, with a total efficiency exceeding 85% across the entire operating bandwidth.

III. BALUN INTEGRATION AND ARRAY EXPERIMENT

A. Design and Integration of Compact Balun

During the fabrication of the array, a compact balun was designed and integrated into the proposed TNP antenna because no commercial RFIC fully covering the n257–n261 bands was available at the lab stage. As a result, a slight bandwidth reduction and a shift were observed in the TNP antenna array. Although various types of 180° hybrid baluns exist [27], they are generally larger than half a wavelength, making them difficult to integrate compactly with the antenna element in an array configuration. In this paper, the four-port 180° hybrid structure introduced in [28] is modified into a three-port hybrid with a small footprint. The narrow balun slot width of 50 μm was feasible using the stackup-PCB fabrication process.

Fig. 7 shows the balun. The transmission phase difference is maintained at a 180° with a maximum error of 0.86° across the entire bandwidth. The average transmission magnitude is 3.89 dB, with a maximum magnitude imbalance of 0.14 dB.

B. Mirror Array Configuration and Measurement

Fig. 8(a) shows the mirrored array configuration of the TNP antenna, integrated with both baluns and connectors. In the process of integrating the balun into the TNP antenna, a balun-to-IDF transition is implemented, as shown in the figure. The mirrored-element arrangement is adopted to achieve higher XPD [29], [30]. At the element level, the TNP antenna inherently exhibits high XPD in the H-plane. As shown in Fig. 8(b), the mirrored array configuration ensures that the surface currents across the E-cut line are equal in magnitude but flow in opposite directions, leading to mutual cancellation in radiation in the E-plane. Fig. 8(c) clearly demonstrates this difference in E-plane XPD between the two configurations. Although Fig. 8(d) shows similar realized gain for both cases, the mirrored configuration is selected due to its significantly

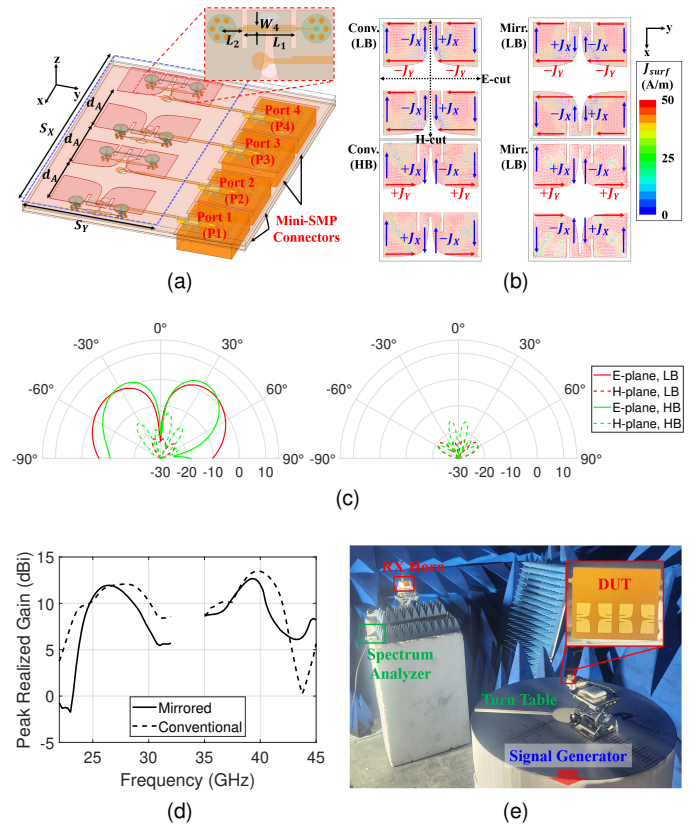


Fig. 8. (a) Illustration of the mirrored array configuration of the TNP antenna, integrated with baluns and connectors. The assigned design parameter values (in mm) are $S_X=19.8$, $S_Y=10$, $d_A=4.9$, $L_1=1.8$, $L_2=0.75$, and $W_4=0.05$. (b) Surface current distribution. (c) Simulated cross-polarized radiation patterns. (b) and (c) are plotted at the center frequencies of the lower band (LB) and higher band (HB), with the conventional configuration on the left and the mirrored configuration on the right. (d) Realized gain versus frequency. (e) Photographs of the fabricated sample and the measurement setup.

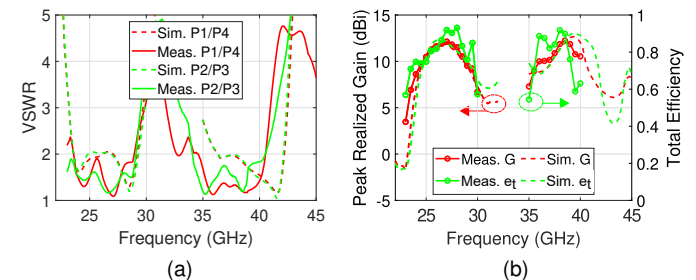


Fig. 9. Simulated and measured (a) VSWR, and (b) peak gain and total efficiency versus frequency for the 1×4 TNP antenna array.

better XPD performance. Fig. 8(e) presents photographs of the fabricated sample and the measurement setup.

Fig. 9(a) shows the simulated and measured differential VSWR of the 1×4 TNP antenna array. The simulated 2:1 VSWR bandwidth of the array in the lower band is 23.7–29.2 GHz (20.8%), while in the higher band it is 36.3–42.1 GHz (14.8%). The measured 2:1 VSWR bandwidth of the array is 23.6–29.0 GHz (20.5%) in the lower band, and 34.6–40.5 GHz (15.7%) in the higher band. The downward shift in the higher band, along with the increased bandwidth in the lower

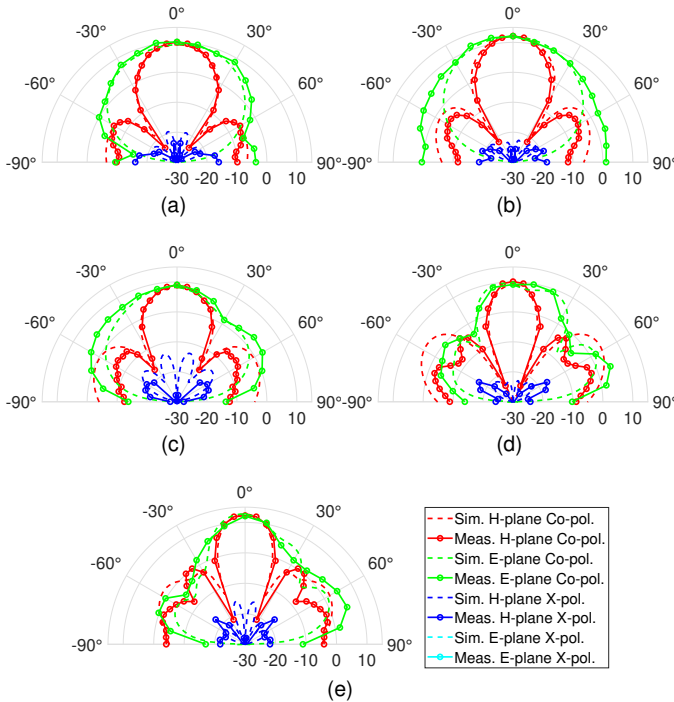


Fig. 10. Simulated (measured) E- and H-plane radiation patterns at (a) 24.25 GHz (24.5 GHz), (b) 26.5 GHz (27.0 GHz), (c) 29.5 GHz (29.5 GHz), (d) 37 GHz (37 GHz), and (e) 39.25 GHz (38.5 GHz).

band, are due to fabrication errors that occurred during in-house manual connector integration using solder paste.

Fig. 9(b) shows the simulated and measured peak gains of the array in the lower band are 11.9 dBi at 26.5 GHz and 12.1 dBi at 27.0 GHz, respectively, while in the higher band they are 12.7 dBi at 39.25 GHz and 12.3 dBi at 38.5 GHz. The figure also presents the simulated and measured total efficiency, which exhibits a similar downward shift in the higher band. The proposed TNP array maintains a total efficiency exceeding 60% across most of the operating bandwidth.

Fig. 10 shows the simulated and measured E- and H-plane radiation patterns at 24.25 (24.25), 26.5 (27.0), 29.5 (29.5), 37 (37), and 39.25 (38.5) GHz, respectively. The array radiation patterns were measured using the active element pattern synthesis technique [6]. Due to the bandwidth limitation of the reference Ka-band horn antenna in our laboratory, gain and radiation pattern measurements were taken only up to 40 GHz. Nonetheless, the accuracy of measurements up to 40 GHz indicates consistent performance beyond that frequency range as well. It is further confirmed that the TNP antenna array provides an excellent simulated and measured XPD of 35 dB, owing to its demonstrated element and array configuration.

Fig. 11 shows that the simulated and measured beam-scanned radiation patterns agree well at the peak gain frequencies in both the lower and higher bands. The simulated and measured -3 dB scan range without grating lobe occurrence is $\pm 45^\circ$ in the lower band and $\pm 34^\circ$ in higher band, respectively.

C. Comparison and Discussion

The antennas proposed in [11] and [13] radiate at the undesired frequency range of 29.5–37 GHz, which lies be-

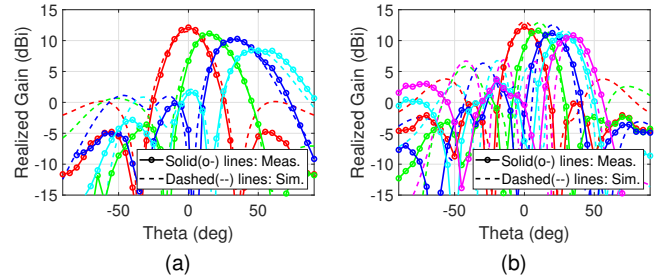


Fig. 11. Simulated (measured) scanned radiation patterns within -3 dB scan range at (a) 26.5 GHz (27 GHz) and (b) 39.25 GHz (38.5 GHz).

TABLE I
COMPARISON OF 5G MMWAVE ANTENNAS THAT FULLY OR NEARLY COVER THE N257–N261 BANDS

Ref.	Frequency bands (GHz)	Peak Realized Gain (dBi)	Element Size (λ_{low}^2)	Array Size (λ_{low}^2)	Profile (λ_{low})
[11]	(A)24-44	(L)9; (H)10	0.44×0.50	2.30×0.50	0.13
[12]	(A)24-30; 37-43.5	(**)(L)7.8; (H)9.0	0.31×0.31	0.62×0.62	0.08
[13]	(A)23.9-43.1	(**)(L)8.6; (H)12.1	0.43×0.43	1.70×1.70	0.12
This work	(E)24.2-29.6 (20.1%); 37.0-44.0 (17.3%)	(L)12.1; (H)12.3	0.39×0.79	1.56×0.79	0.067
	(AS)23.7-29.2 (20.8%); 36.3-42.1 (14.8%)				
	(AM)23.6-29.0 (20.5%); 34.6-40.5 (15.7%)				

* λ_{low} is the free-space wavelength at the lowest operating frequency. (E), (A) (E) and (A) refer to the element and array, respectively. (S), (M) (S) and (M) refer to the simulation and measurement, respectively. (L), (H) (L) and (H) refer to the lower and higher bands, respectively. ** Estimated from the gain-over-frequency plot.

tween the two operational 5G mmWave bands (24.25–29.5 GHz and 37–43.5 GHz), and both have a relatively thick profile of $0.13\lambda_{low}$ and $0.12\lambda_{low}$, respectively. Furthermore, the antennas in [11] and [12] exhibit relatively low array gain, remaining below 10 dBi in both 5G mmWave bands. In contrast, the proposed TNP antenna achieves an element-level dual-wide bandwidth that fully covers the n257–n261 bands, provides a comparable array-level dual-wide bandwidth, delivers the highest array gain in both the lower and higher bands, and maintains the lowest profile. Although the proposed TNP antenna has the largest element size, the overall array size remains acceptable, as it is smaller than that in [13] and comparable to [11].

IV. CONCLUSION

A dual-wideband, low-profile antenna that fully covers the 5G mmWave bands around 28 GHz and 38.5 GHz (n257–n261) is presented. The proposed three-notch patch (TNP) antenna achieves dual-wideband operation by incorporating one hyperbolic notch, two rectangular side notches, and an indirect-differential feeding (IDF) scheme. A high cross-polarization discrimination (XPD) level is attained through careful element and array configurations. Array measurements confirm symmetric radiation patterns and good scan performance in both lower and higher bands.

REFERENCES

- [1] D. Wang *et al.*, "A 24–44 GHz Broadband Transmit–Receive Front End in 0.13- μm SiGe BiCMOS for Multistandard 5G Applications," *IEEE Trans. Microw. Theory Techn.*, vol. 69, no. 7, pp. 3463–3474, July 2021.
- [2] B. Kim and J. Oh, "Single-Glass Layer Optically Transparent Transmitarray With High Aperture Efficiency And Low Profile At 5G Millimeter-Wave Band," *IEEE Trans. Antennas Propag.*, vol. 71, no. 11, pp. 9036–9041, Nov. 2023.
- [3] H. Kim *et al.*, "Independently Polarization Manipulable Liquid- Crystal Based Reflective Metasurface for 5G Reflectarray and Reconfigurable Intelligent Surface," *IEEE Trans. Antennas Propag.*, vol. 71, no. 8, pp. 6606–6616, Aug. 2023.
- [4] S. Bang *et al.*, "Extremely Miniaturized Free-Space Measurement System for RF Metamaterial Composite Based on Beam Focusing Transmitarray," *IEEE Antennas Wireless Propag. Lett.*, vol. 23, no. 6, pp. 1705–1709, June 2024.
- [5] B. Kim and J. Oh, "Characterization of Optically Transparent Two-Metal-Layered Refractive Metasurfaces for 6G Upper-Mid Outdoor-to-Indoor Communication," 2024 *IEEE AP-S/INC-USNC-URSI*, Firenze, Italy, 2024, pp. 1363–1364.
- [6] J. Oh *et al.*, "High-Gain Millimeter-Wave Antenna-in-Display Using Non-Optical Space for 5G Smartphones," *IEEE Trans. Antennas Propag.*, vol. 71, no. 2, pp. 1458–1468, Feb. 2023.
- [7] Q. Chen *et al.*, "A Wideband and Compact Millimeter-Wave Antenna Array Fed by Printed Ridge Gap Waveguide for 5G Applications," *J. Electromagn. Eng. Sci.*, vol. 25, no. 1, pp. 485–493, Jan. 2025.
- [8] J. Park *et al.*, "CMOS Vector Modulator-Based Phase Shifter for Millimeter-Wave Transmitter," *J. Electromagn. Eng. Sci.*, vol. 25, no. 1, pp. 25–31, Jan. 2025.
- [9] S. Bang *et al.*, "Enhancing 2-D Beam Scanning Capability through Extended Transmission Paths in a Liquid Crystal-Based Transmitarray Antenna for mmWave Communications," *J. Electromagn. Eng. Sci.*, vol. 25, no. 1, pp. 85–91, Jan. 2025.
- [10] B. Kim *et al.*, "Locally Optimal Periods in Periodic Optically Transparent Two-Metal-Layered Refractive Metasurfaces for Outdoor-to-Indoor Communication," *IEEE Antennas Wireless Propag. Lett.*, to be published.
- [11] Q. Chen *et al.*, "A Wideband Dual-Polarized Endfire Antenna Array for 5G mm-Wave Smartphones," *IEEE Trans. Antennas Propag.*, vol. 72, no. 2, pp. 1118–1127, Feb. 2024.
- [12] S. J. Yang *et al.*, "Low-Profile Dual-Wideband Dual-Polarized Antenna for 5G Millimeter-Wave Communications," *IEEE Antennas Wireless Propag. Lett.*, vol. 21, no. 12, pp. 2367–2371, Dec. 2022.
- [13] J. Chen *et al.*, "Broadband Cross-Slotted Patch Antenna for 5G Millimeter-Wave Applications Based on Characteristic Mode Analysis," *IEEE Trans. Antennas Propag.*, vol. 70, no. 12, pp. 11277–11292, Dec. 2022.
- [14] J. Seo *et al.*, "Miniaturized Dual-Band Broadside/Endfire Antenna-in-Package for 5G Smartphone," *IEEE Trans. Antennas Propag.*, vol. 69, no. 12, pp. 8100–8114, Dec. 2021.
- [15] X. Zhang *et al.*, "A Wideband Dual-Polarized Antenna-in-Package for 5G Millimeter-Wave User Equipment," *IEEE Trans. Compon., Packag., Manuf. Technol.*, vol. 14, no. 10, pp. 1845–1853, Oct. 2024.
- [16] A. E. Farahat and K. F. A. Hussein, "Dual-Band (28/38 GHz) Wideband MIMO Antenna for 5G Mobile Applications," *IEEE Access*, vol. 10, pp. 32213–32223, 2022.
- [17] B. Kim *et al.*, "Heterogeneous Metasurface Empowering Proximate High-Permittivity Ceramic Cover for a 5G Dual-Band Millimeter-Wave Smartphone," *IEEE Trans. Antennas Propag.*, vol. 72, no. 5, pp. 4086–4094, May 2024.
- [18] X. Yin *et al.*, "Millimeter-Wave Dual-Band Filtering Patch Antenna and MIMO Array Using Multinull Resonator," *IEEE Trans. Antennas Propag.*, vol. 72, no. 9, pp. 6897–6907, Sep. 2024.
- [19] D. Lee *et al.*, "Dual-Polarized Dual-Band Antenna-on-Display Using Via-Less and Single-Layer Topology for mmWave Wireless Scenarios," *IEEE Antennas Wireless Propag. Lett.*, vol. 22, no. 5, pp. 1000–1004, May 2023.
- [20] F. Sun *et al.*, "A Millimeter-Wave Wideband Dual-Polarized Antenna Array With 3-D-Printed Air-Filled Differential Feeding Cavities," *IEEE Trans. Antennas Propag.*, vol. 70, no. 2, pp. 1020–1032, Feb. 2022.
- [21] Y. Zhang *et al.*, "Broadband Dual-Polarized Differential-Fed Filtering Antenna Array for 5G Millimeter-Wave Applications," *IEEE Trans. Antennas Propag.*, vol. 70, no. 3, pp. 1989–1998, March 2022.
- [22] S. Liao *et al.*, "Differentially Fed Planar Aperture Antenna With High Gain and Wide Bandwidth for Millimeter-Wave Application," *IEEE Trans. Antennas Propag.*, vol. 63, no. 3, pp. 966–977, March 2015.
- [23] M. Alzidani *et al.*, "Ultra-Wideband Differential Fed Hybrid Antenna With High-Cross Polarization Discrimination for Millimeter Wave Applications," *IEEE Access*, vol. 8, pp. 80673–80683, 2020.
- [24] Y. Li, Z. Zhao, Z. Tang and Y. Yin, "Differentially Fed, Dual-Band Dual-Polarized Filtering Antenna With High Selectivity for 5G Sub-6 GHz Base Station Applications," *IEEE Trans. Antennas Propag.*, vol. 68, no. 4, pp. 3231–3236, April 2020.
- [25] P. S. Bakariya, S. Dwari, M. Sarkar and M. K. Mandal, "Proximity-Coupled Multiband Microstrip Antenna for Wireless Applications," *IEEE Antennas Wireless Propag. Lett.*, vol. 14, pp. 646–649, 2015.
- [26] H. Kim and J. Oh, "140-GHz Wideband Array Antenna-in-Package Using Multimode Resonance," *IEEE Trans. Antennas Propag.*, vol. 71, no. 3, pp. 2136–2144, March 2023.
- [27] H. -x. Xu, G. -m. Wang and K. Lu, "Microstrip Rat-Race Couplers," *IEEE Microw. Mag.*, vol. 12, no. 4, pp. 117–129, June 2011.
- [28] M. E. Bialkowski and Y. Wang, "Wideband Microstrip 180° Hybrid Utilizing Ground Slots," *IEEE Microw. Wireless Compon. Lett.*, vol. 20, no. 9, pp. 495–497, Sept. 2010.
- [29] J. Granholm and K. Woelders, "Dual polarization stacked microstrip patch antenna array with very low cross-polarization," *IEEE Trans. Antennas Propag.*, vol. 49, no. 10, pp. 1393–1402, Oct. 2001.
- [30] W. -Y. Liu *et al.*, "A Low-Cross-Polarization and Wide-Scanning-Range Dual-Polarized Planar Phased Array Using Mirrored Pair Feeding Technique," *IEEE Antennas Wireless Propag. Lett.*, vol. 23, no. 6, pp. 1749–1753, Jun. 2024.